
ANOMALOUS KLEIN TUNNELLING WITH MAGNETIC BARRIERS IN STRAINED GRAPHENE

A PREPRINT

 **Edgardo Marin-Colli**^{†,1},  **Tonatiuh Gómez-Ramírez**^{†,2},  **O-Excell Gutierrez**^{*,3},
 **Yonatan Betancur-Ocampo**^{*,4},  **Alfredo Raya**^{**,***,5} and  **Erik Díaz-Bautista**^{†,6}

[†]Escuela Superior de Física y Matemáticas, Instituto Politécnico Nacional, 07738 Mexico City, Mexico

^{*}Facultad de Ciencias, Universidad Autónoma de Baja California, 22860, Ensenada, Baja California, México

^{*}Instituto de Física, Universidad Nacional Autónoma de México, Ciudad de México, México

^{**}Facultad de Ingeniería Eléctrica, Universidad Michoacana de San Nicolás de Hidalgo, 58040 Morelia, Michoacán, México

^{***}Centro de Ciencias Exactas, Universidad del Bío-Bío. Casilla 447, Chillán, Chile

e-mail: emarinc2200@alumno.ipn.mx¹, agomezr2201@alumno.ipn.mx², oscar.gutierrez22@uabc.edu.mx³, ybetancur@fisica.unam.mx⁴, alfredo.raya@umich.mx⁵, ediazba@ipn.mx⁶

ABSTRACT

We study electron transport in a strained graphene sheet subjected to a sequence of N electrostatic and magnetic barriers. Employing a modified and improved transfer-matrix framework, we examine how the transmission and reflection coefficients evolve with variations in uniaxial strain and in the number of barriers. The interplay of mechanical deformation and external magnetic fields is found to generate an anomalous Klein tunnelling, allowing the conductance to be effectively modulated through strain and barrier configurations. These findings highlight the role of strain engineering and magnetic field modulation as powerful tools for tailoring charge transport in two-dimensional materials. More broadly, they underscore how mechanical and electromagnetic control can be used to design next-generation solid-state devices with tunable electronic properties.

Keywords electron transmission · transfer matrix · strained graphene · magnetic and electrostatic barriers

1 Introduction

With the discovery of graphene, it became possible to explore Klein tunnelling experimentally — a relativistic effect originally predicted by Oskar Klein in 1929 [1] that consists in a relativistic particle to tunnel with certainty regardless of the height and the width of the barrier. In graphene, charge carriers behave as massless Dirac fermions moving at a Fermi velocity v_F nearly 300 times slower than the speed of light [2]. This property, together with the conservation of pseudo-spin, allowed perfect electron transmission through electrostatic barriers, even when the potential height exceeds the carrier energy [3–5]. The conservation of pseudo-spin forbids backscattering at normal incidence, leading to a transmission coefficient $T = 1$ [3].

The experimental realization of Klein tunnelling in graphene p-n junctions marked a transformational moment in condensed matter physics [5,6]. These experiments provided direct evidence of perfect transmission through engineered potential barriers, confirming theoretical predictions about the chiral nature of graphene quasiparticles. Subsequent work demonstrated conductance oscillations in narrow graphene heterojunctions, where the phase shift observed in the conductance fringes at low magnetic fields constituted a signature of the absence of backscattering at normally incident carriers [5]. These findings established graphene as an accessible platform for studying quantum electrodynamic phenomena that would be impractical to observe with elementary particles.

Beyond this ideal scenario, more complex configurations such as magnetic fields, strain, or periodic potentials can alter the transmission properties, giving rise to anomalous Klein tunnelling, where perfect transmission occurs at nonzero incidence angles or specific energy ranges [7,8]. Strain engineering, in particular, has emerged as a powerful tool for modulating the electronic properties of graphene. Uniaxial strain can open a bandgap at the Dirac points, with tensile

strains that can open band gap beyond 23% along the zig-zag direction [9], while combinations of shear and uniaxial strain can achieve bandgap modulations from 0 to 0.9 eV under deformations of 12-17% [10, 11]. The interplay between mechanical deformation and external magnetic fields introduces additional degrees of freedom for controlling transport properties, enabling the emergence of valley-dependent phenomena and pseudomagnetic fields that further enrich the physics of electron transmission [10, 12].

Graphene superlattices, consisting of periodic arrays of electrostatic and magnetic barriers, have attracted considerable attention as platforms for investigating transmission resonances and filtering properties [13–15]. The transfer matrix method has proven to be an essential theoretical tool for analyzing transport through these multi-barrier systems, allowing for the systematic study of how structural parameters such as barrier height, width, and periodicity affect the transmission spectrum [15, 16]. Non-conventional superlattice profiles, including Gaussian and Lorentzian potential distributions, have demonstrated the ability to create nearly perfect pass bands and omnidirectional filtering characteristics [15]. These findings suggest potential applications in electron beam collimation, energy filtering, and valleytronic devices.

In this work, we study this phenomenon using a graphene superlattice model [13, 14, 16–20] composed of N electrostatic and δ -magnetic barriers arranged along the x -axis. This approach enables us to investigate how mechanical deformation and field modulation affect the transmission resonances ($T = 1$), providing a framework to control and interpret both Klein and anomalous Klein tunnelling in graphene-based systems. The prospect of manipulating electron transport through the combined effects of strain and δ -magnetic fields opens new pathways toward graphene-based electronic devices, including high-frequency transistors, quantum computing platforms, and flexible electronics [21–23]. We organize the remaining of this article as follows: In Sect. 2 we construct the effective Hamiltonian for uniaxially strained graphene. Section 3 is devoted to the discussion of the transfer matrix framework we employ in our study. In Sect. 4 we present and discuss the results for the transmission coefficient T and conductance G for different barrier configurations. Conclusions are drawn at the end, in Sect. 5.

2 Effective Dirac Hamiltonian for uniaxially strained graphene

Graphene is a two-dimensional Dirac material well-known in condensed matter physics due to its unique electronic, optical and mechanical properties. It consists of a honeycomb-like lattice composed of carbon atoms and is described by the lattice vectors \vec{a}_1 and \vec{a}_2 shown in Fig. 1. The graphene unit cell contains two carbon atoms, each of which belongs to a triangular sublattice, labelled as A or B. In pristine graphene, as well as strained graphene [9, 24–26], the tight-binding (TB) Hamiltonian that describes the hop of an electron to the nearest atom [26–28], i.e., from an atom in the sublattice A (B) to another one in sublattice B (A), is obtained analyzing the reciprocal lattice, where second-nearest neighbor interactions and p_z orbital overlap are neglected. From the Bloch theorem, such a Hamiltonian turns out to be [26, 27, 29]:

$$H_{\text{TB}} = \sum_{j=1}^3 \begin{pmatrix} 0 & t_j e^{i\vec{k} \cdot \vec{\delta}_j} \\ t_j e^{-i\vec{k} \cdot \vec{\delta}_j} & 0 \end{pmatrix}, \quad (1)$$

being its energy spectrum

$$E_{\pm} = \lambda \left(\sum_{i=1}^3 t_i^2 + 2 \sum_{i<j} t_i t_j \cos(\vec{k} \cdot (\delta_i - \delta_j)) \right)^{1/2}, \quad (2)$$

where $\lambda = \text{sgn}(E)$ denotes the conduction ($\lambda = +1$) and valence ($\lambda = -1$) energy bands, $\vec{k} = (k_x, k_y)$ is the wave vector of electron, while t_1 and t_2 are two hopping parameters that quantify the probability amplitude that an electron hops to the nearest atom. In the strained graphene case, t_j vary with uniaxial strain ϵ through an exponential dependence on the modified bond lengths δ_j , $j = 1, 2, 3$, namely, $t_j = t e^{-\beta(\delta_j/a_0 - 1)}$, where $\beta = 2.6$ is the Grüneisen constant, $t = 2.7$ eV is the hopping in pristine graphene and $a_0 = 1.42$ Å is the bond length in the undeformed sheet of the material [9, 26, 30, 31]. Here, the tensile strain ϵ quantifies the percentage of deformation [9] and is proportional to the magnitude of a uniaxial tension T applied to a graphene layer along zigzag (\mathcal{ZZ}) or armchair (\mathcal{AC}) direction (see again Fig. 1).

More precisely, the nearest-neighbor sites, $\vec{\delta}_1 = 2\vec{a}_1/3 - \vec{a}_2/3$, $\vec{\delta}_2 = 2\vec{a}_2/3 - \vec{a}_1/3$, and $\vec{\delta}_3 = -\vec{\delta}_1 - \vec{\delta}_2$, are related to the tensile strain through the deformed lattice vectors given by [32]:

$$\vec{a}_1 = \sqrt{3} a_0 \left[(1 + \rho^+ \epsilon + \rho^+ \epsilon \cos(2\zeta)) \mathbf{e}_x + \rho^+ \epsilon \sin(2\zeta) \mathbf{e}_y \right], \quad (3)$$

$$\vec{a}_2 = \frac{\sqrt{3}}{2} a_0 \left[(1 + \rho^- \epsilon + 2\rho^+ \epsilon \cos(2\zeta - \pi/3)) \mathbf{e}_x + (\sqrt{3}(1 + \rho^- \epsilon) + 2\rho^+ \epsilon \sin(2\zeta - \pi/3)) \mathbf{e}_y \right], \quad (4)$$

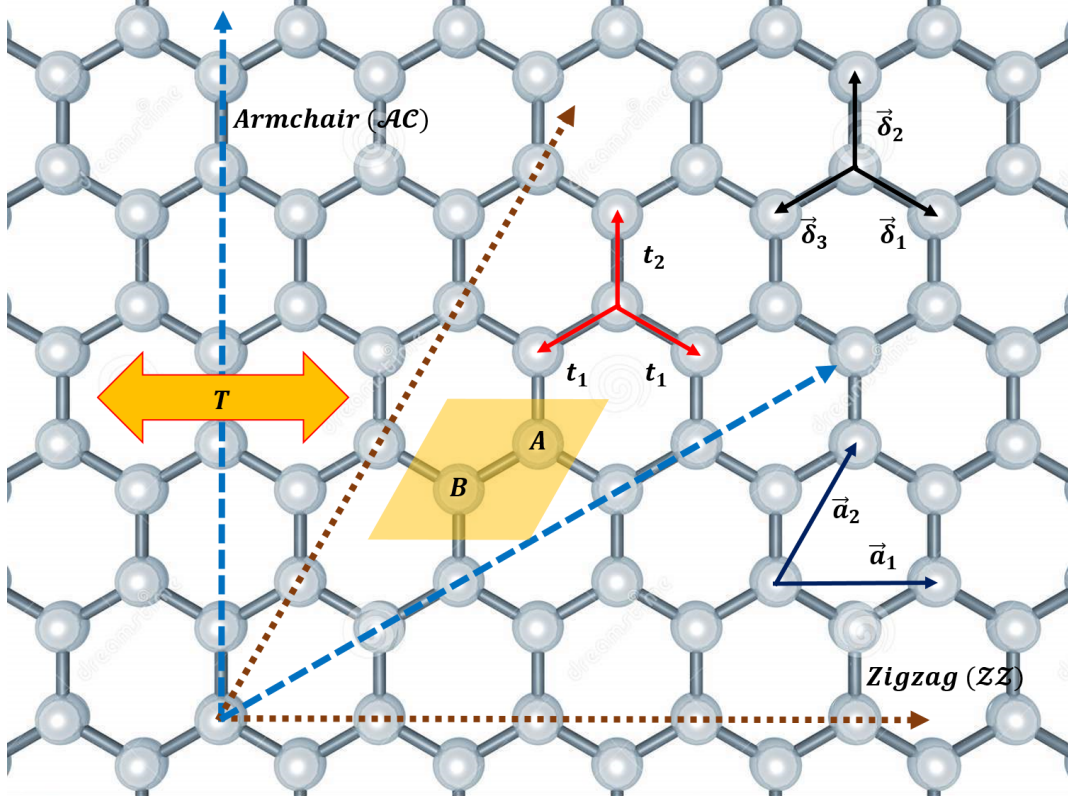


Figure 1: Uniaxially strained graphene is considered with the zigzag (armchair) direction aligned along the x -axis (y -axis), alternating every 30° . Strain along these high-symmetry directions modifies the nearest-neighbor hopping amplitudes to two distinct values, t_1 and t_2 . The nearest-neighbor positions are given by $\vec{\delta}_1$, $\vec{\delta}_2$, and $\vec{\delta}_3$, while the lattice vectors \vec{a}_1 and \vec{a}_2 span the deformed hexagonal structure. The unit cell is colored in yellow.

where $\rho^\pm = (1 \pm \nu)/2$, being $\nu \sim 0.165$ the Poisson ratio of graphene [33, 34], and ζ indicates the direction along the uniaxial strain ϵ is applied. Therefore, for ZZ deformations ($\zeta = 0^\circ$), we have that

$$\delta_1^{ZZ} = \delta_3^{ZZ} = a_0 \sqrt{\left(1 + \frac{1}{4}(3 - \nu)\epsilon\right)^2 + \frac{3}{16}(1 + \nu)^2 \epsilon^2}, \quad \delta_2^{ZZ} = a_0(1 - \nu\epsilon), \quad (5)$$

while for AC deformations ($\zeta = 90^\circ$), we get

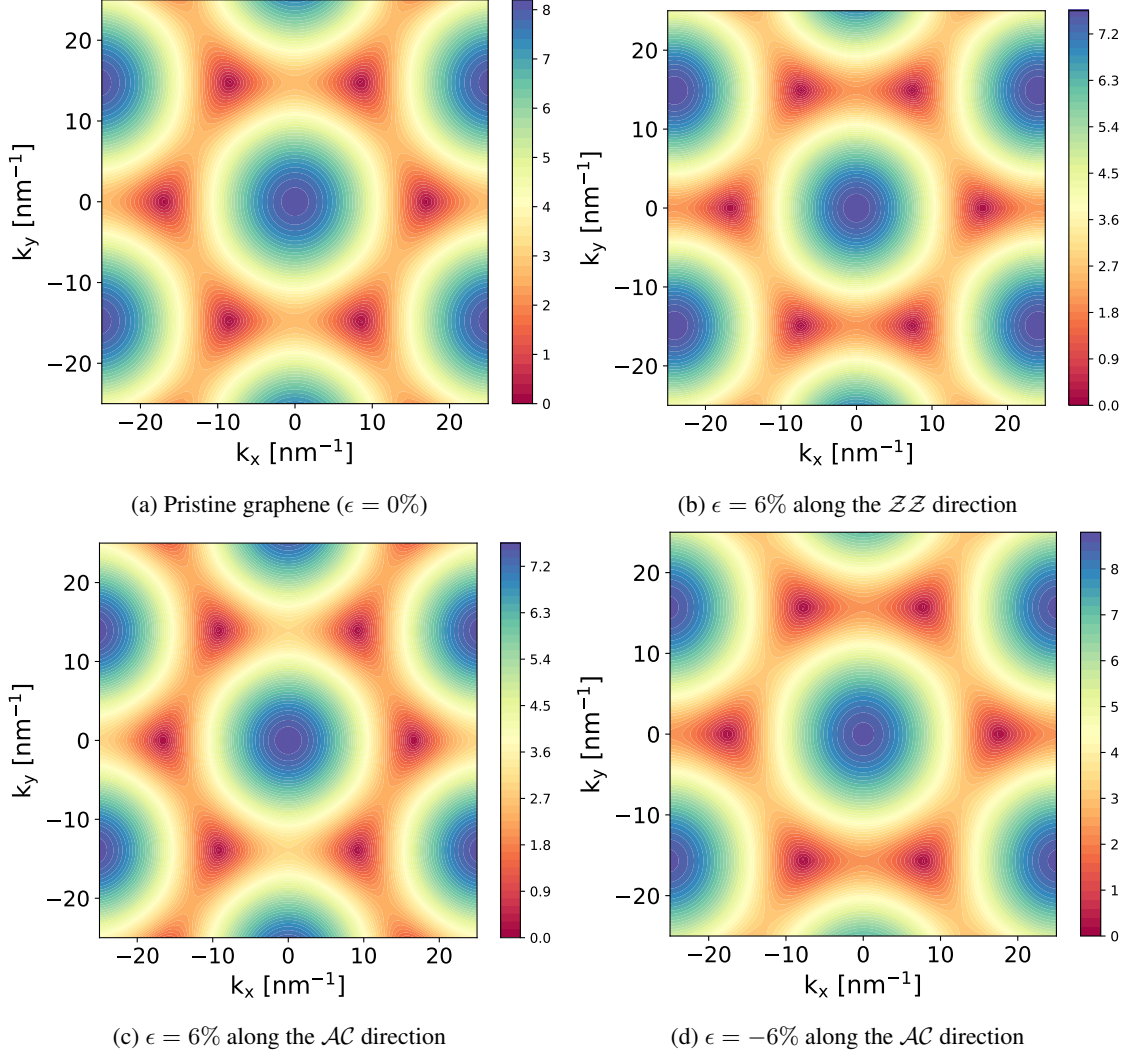
$$\delta_1^{AC} = \delta_3^{AC} = a_0 \sqrt{\left(1 + \frac{1}{4}(1 - 3\nu)\epsilon\right)^2 + \frac{3}{16}(1 + \nu)^2 \epsilon^2}, \quad \delta_2^{AC} = a_0(1 + \epsilon). \quad (6)$$

Now, expanding the TB Hamiltonian (1) around the Dirac point position \vec{K}_D at the first Brillouin zone (see Fig. 2), i.e. by taking $\vec{k} = \vec{p} + \vec{K}_D$ such that $|\vec{p}| \ll |\vec{K}_D|$, and where the following relation is fulfilled

$$\sum_j^3 t_j \exp(-i\vec{K}_D \cdot \vec{\delta}_j) = 0 \quad \implies \quad \cos[\vec{K}_D \cdot (\vec{\delta}_1 - \vec{\delta}_2)] = -\frac{t_2}{2t_1}, \quad (7)$$

the effective Dirac-like Hamiltonian in the continuum approximation is given by

$$H = v_x p_x \sigma_x + v_y p_y \sigma_y, \quad (8)$$

Figure 2: Energy contour of the conduction band in (2) near the first Brillouin zone for different strain values ϵ .

where $\sigma_{x/y}$ are the Pauli matrices and

$$v_x = \frac{1}{\hbar} \sum_{j=1}^3 \delta_{jx} t_j \sin(\vec{K}_D \cdot \vec{\delta}_j) = \frac{1}{\hbar} \sqrt{a_{1x}^2 t_1^2 + (a_{2x} - a_{1x}) a_{2x} t_2^2}, \quad (9)$$

$$v_y = \frac{1}{\hbar} \sum_{j=1}^3 \delta_{jy} t_j \cos(\vec{K}_D \cdot \vec{\delta}_j) = \frac{1}{\hbar} \sqrt{a_{1y}^2 t_1^2 + (a_{2y} - a_{1y}) a_{2y} t_2^2}, \quad (10)$$

are the components of the Fermi velocity.

Then, from the Schrödinger equation

$$H\Psi(\vec{r}, \vec{k}) = \hbar \begin{pmatrix} 0 & g^*(\vec{k}) \\ g(\vec{k}) & 0 \end{pmatrix} \Psi(\vec{r}, \vec{k}) = E\Psi(\vec{r}, \vec{k}), \quad (11)$$

where E denotes the energy and the function $g(\vec{k}) = g_x(\vec{k}) + ig_y(\vec{k}) = v_x k_x + iv_y k_y$, we write the solution as:

$$\Psi(\vec{r}, \vec{k}) = \frac{1}{\sqrt{2}} \begin{pmatrix} 1 \\ \lambda e^{i\theta(\vec{k})} \end{pmatrix} e^{ik_x x} e^{ik_y y}, \quad E = \lambda \hbar \sqrt{v_x^2 k_x^2 + v_y^2 k_y^2}. \quad (12)$$

Here,

$$\theta(\vec{k}) = \arctan\left(g_y(\vec{k})/g_x(\vec{k})\right), \quad (13)$$

is the so-called pseudo-spin angle, while wave vector direction is denoted by

$$\gamma(\vec{k}) = \arctan(k_y/k_x). \quad (14)$$

It is worth mentioning that the group velocity direction, given by

$$\phi(\vec{k}) = \arctan\left(\partial_{k_y}|g(\vec{k})|/\partial_{k_x}|g(\vec{k})|\right), \quad (15)$$

indicates the direction of the electron beam in the scattering process and therefore, for anisotropic materials such as strained graphene [26, 35], the angles $\theta(\vec{k})$, $\gamma(\vec{k})$, and $\phi(\vec{k})$ are not generally parallel, which have lead to the explanation of anomalous Klein tunnelling in strained graphene due to the conservation of pseudo-spin $\theta(\vec{k})$, while $\phi(\vec{k})$ follows an anisotropic Snell's law.

It is worth mentioning that the effective Dirac Hamiltonian derived above is valid in the long-wavelength limit, where the electron wavelength is much larger than the lattice constant $a_c = \sqrt{3}a_0 \sim 0.25$ nm and the spatial variations of external potentials occur on length scales significantly exceeding the interatomic distances. In this regime, the two inequivalent valleys \vec{K}_D and \vec{K}'_D in the first Brillouin zone remain decoupled, and intervalley scattering is negligible [3, 30]. For these reasons, we shall assume that both the electrostatic potential $V(x)$ and the magnetic vector potential $A_y(x)$ considered in this work vary smoothly over distances of several nanometers. While we model magnetic barriers using Dirac delta functions for analytical tractability, these should be understood as representing sharp but finite-width transitions occurring over length scales ~ 5 – 10 nm, which is sufficient to prevent significant valley mixing [36, 37]. In this way, the δ -function idealization captures the essential physics of abrupt magnetic field changes while maintaining mathematical simplicity.

Similarly, the strain fields shall be assumed to vary smoothly across the sample, consistent with the continuum elasticity theory employed in Eqs. (3)–(6) [38]. Atomic-scale disorder or defects, which could induce intervalley scattering, are not included in the present model. The results presented here thus apply to high-quality graphene samples where such disorder is minimal, as achieved in modern experiments on exfoliated or CVD-grown graphene [39, 40].

On the other hand, for potential variations on atomic length scales or in the presence of strong disorder, a full tight-binding treatment or atomistic simulations would be required to properly account for valley mixing effects [41, 42]. Nevertheless, the continuum Dirac model employed here has been extensively validated against experiments and provides accurate predictions for transport properties in the regime where valley mixing is suppressed.

3 Transfer matrix framework

Now, let us consider an electron in strained graphene under the interaction of a multiple-barrier structure of N electrostatic potentials $V(x)$ and magnetic fields $\vec{B}(x)$. Assuming the Landau gauge $\vec{A}(x) = A_y(x)\mathbf{e}_y$, the corresponding Hamiltonian is given by [35, 43–46]

$$H = \hbar(v_x\sigma_x p_x + v_y\sigma_y(p_y + eA_y(x))) + V(x)\sigma_0, \quad (16)$$

where

$$V(x) = \begin{cases} V_0, & x_{2n-2} < x < x_{2n-1}, \\ 0, & \text{otherwise,} \end{cases} \quad A_y(x) = B\ell_B(\Theta(x - x_{2n-2}) - \Theta(x - x_{2n-1})), \quad (17)$$

for $n = 1, 2, \dots, (N+1)/2$. Here, $D = x_{2n-1} - x_{2n-2}$ is the width of the n -th region, N indicates the number of regions and $\ell_B = \sqrt{\hbar/(eB)}$ is the magnetic length (see Fig. 3). The function $\Theta(x)$ denotes the Heaviside step function, so that

$$\vec{B}(x) = \nabla \times \vec{A}(x) = B\ell_B(\delta(x - x_{n-1}) - \delta(x - x_n))\mathbf{e}_z, \quad (18)$$

i.e., this corresponds to a pair of oppositely directed δ -function magnetic barriers of strength B and separated by a distance D . The choice of the vector potential $\vec{A}(x)$ as in (17) guarantees that it is constant in each interval $x_{2n-1} < x < x_{2n-2}$.

As mentioned, the δ -function magnetic barriers described in Eq. (18) constitute an idealization that facilitates the analytical and semi-analytical treatment of the transport problem. In reality, magnetic field profiles with vanishingly small width cannot be achieved, and any experimental realization would involve finite spatial extent. Nevertheless, this

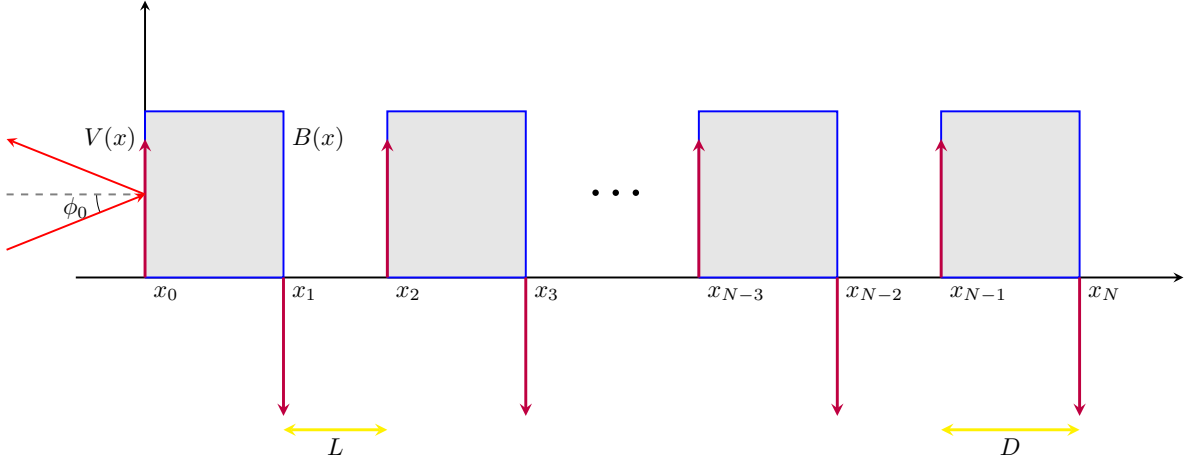


Figure 3: Diagram of the system of N magnetic and electrostatic barriers disposed along the x axis on a material surface.

idealization serves a dual purpose: (i) it provides mathematical tractability, enabling us to derive exact or semi-exact solutions via the transfer matrix method, and (ii) it captures the essential physics of abrupt magnetic field transitions that can be engineered in graphene-based devices.

For the magnetic field strengths considered in this work ($B \sim 0.1\text{--}0.2$ T), the magnetic length $\ell_B = \sqrt{\hbar/(eB)}$ defines the characteristic scale for magnetic confinement. If the actual magnetic barrier width D satisfies $D \ll \ell_B$, the δ -function approximation provides a reasonable first-order description of the transport physics. However, for barrier widths comparable to or exceeding ℓ_B , more complex effects emerge. In particular, the formation of Landau levels within the barrier regions becomes relevant, and the electronic states acquire characteristics of quantum dot confinement with a discretized energy spectrum [47].

Then, to implement the transfer matrix approach, we propose the wave function *ansatz* inside the n -th region as

$$\begin{aligned} \Phi_n(\vec{r}) &= t_n \Psi(\vec{r}, \vec{k}_n^t) + r_n \Psi(\vec{r}, \vec{k}_n^r) \\ &= \frac{e^{ik_y y}}{\sqrt{2}} \begin{pmatrix} e^{ik_{n,x}^t x} & e^{ik_{n,x}^r x} \\ \lambda_n e^{i(\theta(k_{n,x}^t) + k_{n,x}^t x)} & \lambda_n e^{i(\theta(k_{n,x}^r) + k_{n,x}^r x)} \end{pmatrix} \begin{pmatrix} t_n \\ r_n \end{pmatrix} = \frac{e^{ik_y y}}{\sqrt{2}} M_n(x) \begin{pmatrix} t_n \\ r_n \end{pmatrix}, \end{aligned} \quad (19)$$

where t_n and r_n are the transmitted and reflected wave amplitudes, respectively. For the first region ($n = 0$), $t_0 = 1$ corresponds to the incident wave, with an incident wave vector \vec{k}_0^t , and $r_0 = r$ for the reflected part and wave vector \vec{k}_0^r . Notice that $n = N + 1$ in the last region, and thus $r_{N+1} = 0$ because there is no reflection and $t_{N+1} = t$ for the outgoing wave. In addition, we define the dynamical quantities:

$$k_{x,n}^{(t/r)} = (+/-) \lambda_n \sqrt{\left(\frac{E - V(x)}{\hbar v_x}\right)^2 - \frac{v_y^2}{v_x^2} \left(k_{y,0} + \frac{eA_y(x)}{\hbar}\right)^2}, \quad (20)$$

$$k_{y,0} = \frac{v_x |E| \tan(\phi_0)}{\hbar v_y^2 \sqrt{1 + \left(\frac{v_x \tan(\phi_0)}{v_y}\right)^2}}, \quad (21)$$

$$\theta(\vec{k}_n^{(t/r)}) = \arctan \left(\frac{v_y \left(k_{y,0} + \frac{eA_y(x)}{\hbar}\right)}{v_x k_{x,n}^{(t/r)}} \right), \quad (22)$$

where $\phi_0 \equiv \phi(\vec{k}_0^t)$ is the incidence angle at the first barrier obtained from (15).

Now, by imposing the continuity condition at the position $x = x_n$ that separates the regions with wave functions $\Phi_n(\vec{r})$ and $\Phi_{n+1}(\vec{r})$,

$$\Phi_n(x_n) = \Phi_{n+1}(x_n), \quad (23)$$

we obtain the following relation

$$\begin{pmatrix} t_n \\ r_n \end{pmatrix} = M_n^{-1}(x_n)M_{n+1}(x_n) \begin{pmatrix} t_{n+1} \\ r_{n+1} \end{pmatrix},$$

where the matrices $M_m(x_l)$ are

$$M_m(x_l) = \frac{1}{\sqrt{2}} \begin{pmatrix} e^{ik_{x,m}^t x_l} & e^{ik_{x,m}^r x_l} \\ \lambda_m e^{i(\theta(\vec{k}_m^t) + k_{x,m}^t x_l)} & \lambda_m e^{i(\theta(\vec{k}_m^r) + k_{x,m}^r x_l)} \end{pmatrix}. \quad (24)$$

Now, considering the part of the system consisting of N regions, it follows that

$$\Phi_0(\vec{r}) = M_1(x_0)M_1^{-1}(x_1)M_2(x_2)M_2^{-1}(x_3) \cdots M_N(x_{N-1})M_N^{-1}(x_N)\Phi_{N+1}(\vec{r}), \quad (25)$$

from where we can define the effective transfer matrix as

$$\Lambda = \prod_{n=1}^N M_n(x_{n-1})M_n^{-1}(x_n), \quad (26)$$

being

$$\begin{aligned} & M_n(x_{n-1})M_n^{-1}(x_n) \\ &= \frac{1}{e^{i\theta(\vec{k}_n^r)} - e^{i\theta(\vec{k}_n^t)}} \begin{pmatrix} e^{i(\theta(\vec{k}_n^r) - \xi_{nn-1}^t)} - e^{i(\theta(\vec{k}_n^t) - \xi_{nn-1}^r)} & \lambda_n (e^{-i\xi_{nn-1}^r} - e^{-i\xi_{nn-1}^t}) \\ \lambda_n e^{i(\theta(\vec{k}_n^t) + \theta(\vec{k}_n^r))} (e^{-i\xi_{nn-1}^t} - e^{-i\xi_{nn-1}^r}) & e^{i(\theta(\vec{k}_n^r) - \xi_{nn-1}^r)} - e^{i(\theta(\vec{k}_n^t) - \xi_{nn-1}^t)} \end{pmatrix}, \quad (27) \end{aligned}$$

and $\xi_{nn-1}^{(r/t)} = k_{x,n}^{(r/t)}(x_n - x_{n-1})$ is the phase shift for the outgoing wave in the n -th region. The latter expression can also be expressed in terms of the propagation P_n and dynamics D_n matrices as

$$M_n(x_{n-1})M_n^{-1}(x_n) = D_n P_n D_n^{-1}, \quad (28)$$

where

$$P_n = \begin{pmatrix} e^{-ik_{x,n}^t(x_n - x_{n-1})} & 0 \\ 0 & e^{-ik_{x,n}^r(x_n - x_{n-1})} \end{pmatrix}, \quad D_n = \begin{pmatrix} 1 & 1 \\ \lambda_n e^{i\theta(\vec{k}_n^t)} & \lambda_n e^{i\theta(\vec{k}_n^r)} \end{pmatrix}. \quad (29)$$

The previous matrix transfer framework allows us to simplify the electron scattering across the stratified potential barriers, where it is only necessary to solve a 2×2 linear equation system to quantify the transmission probability of the electron crossing the whole set of barriers

$$\Lambda \begin{pmatrix} 1 \\ \lambda_{N+1} e^{i\theta(\vec{k}_{N+1}^t)} \end{pmatrix} e^{ik_{x,N+1}^t x_N} t = \begin{pmatrix} 1 \\ \lambda_0 e^{i\theta(\vec{k}_0^t)} \end{pmatrix} + r \begin{pmatrix} 1 \\ \lambda_0 e^{i\theta(\vec{k}_0^r)} \end{pmatrix}, \quad (30)$$

we find the squared modulus of transmission t and reflection r amplitudes as:

$$T = |t|^2 = \frac{4 \sin^2 \left(\frac{1}{2} (\theta(\vec{k}_0^t) - \theta(\vec{k}_0^r)) \right)}{|\rho_y - \lambda_0 \rho_x e^{i\theta(\vec{k}_0^r)}|^2}, \quad R = |r|^2 = \frac{|\rho_y - \lambda_0 \rho_x e^{i\theta(\vec{k}_0^t)}|^2}{|\rho_y - \lambda_0 \rho_x e^{i\theta(\vec{k}_0^r)}|^2}, \quad (31)$$

where

$$\begin{pmatrix} \rho_x \\ \rho_y \end{pmatrix} = \Lambda \begin{pmatrix} 1 \\ \lambda_{N+1} e^{i\theta(\vec{k}_{N+1}^t)} \end{pmatrix}. \quad (32)$$

3.1 Conductance

The conductance is a physical quantity defined as the inverse of resistance; therefore, its study provides important insights into the combined effects of the magnetic field and uniaxial strain on electronic transport in graphene. Based on the Landauer–Büttiker formalism, the conductance per unit length is calculated as [48–50]

$$G = \frac{e^2}{\hbar} \int T dk = \frac{G_0}{\pi} \int_{-\pi/2}^{\pi/2} T \frac{\sec^2(\phi_0)}{\left(1 + \frac{v_x^2}{v_y^2} \tan^2(\phi_0)\right)^{3/2}} d\phi_0, \quad (33)$$

where

$$G_0 = \frac{e^2 |E| v_x}{\hbar^2 v_y^2}. \quad (34)$$

This formalism, which has become a cornerstone in mesoscopic physics, treats electron transport as a scattering problem at the Fermi level, where the conductance is determined by the transmission probability of electrons between reservoirs [50, 51]. The approach is particularly suited for graphene systems, where phase-coherent transport can be maintained over micron-scale distances at low temperatures, and where the chiral nature of charge carriers leads to unique transmission properties [3, 52].

In the context of Klein tunnelling, the conductance exhibits distinctive features that directly reflect the anomalous transmission properties of Dirac fermions through potential barriers. Experimental measurements in graphene p-n junctions have demonstrated conductance oscillations that constitute direct signatures of Klein tunnelling [5, 6]. These oscillations arise from Fabry-Pérot resonances within the junction cavity, and their phase shift under low magnetic fields provides unambiguous evidence of the perfect transmission of normally incident carriers [5]. The resistance across steep potential steps has been shown to quantitatively agree with theoretical predictions of Klein tunnelling for Dirac fermions, confirming the validity of the Landauer-Büttiker description in this regime [6, 53].

The application of external magnetic fields introduces additional complexity to the conductance behavior. Magnetic barriers deflect the angular dependence of electron transmission, suppressing normally incident electrons and reducing overall conductance [54, 55]. When the magnetic field strength exceeds a critical value corresponding to the cyclotron orbit diameter matching the barrier width, conductance can be suppressed to nearly zero regardless of the potential barrier height, effectively achieving confinement of Dirac fermions [54]. This magnetic field-induced conductance modulation has been proposed as a mechanism for electro-optic applications and valleytronic devices [12, 55]. The interplay between magnetic barriers and electrostatic potentials generates distinct Fabry-Pérot fringe patterns in the conductance, with characteristic constriction regions appearing when the barrier height approaches the Fermi energy [54].

On the other hand, uniaxial strain provides an additional degree of freedom for conductance modulation in graphene systems. Strain engineering can open transport gaps at grain boundaries and interfaces, significantly affecting the on-off ratio in potential transistor applications [56, 57]. The modulation of conductance depends sensitively on the topological structure of the boundaries, the strain direction, and the twist angle between misoriented graphene layers [56, 57]. In vertical graphene heterostructures, strain-induced displacement of Dirac cones can create conduction gaps as large as a few hundred meV with only a few percent strain, leading to strong conductance modulation and significant enhancement of the Seebeck coefficient [57]. Recent theoretical work predicts that strain-modulated graphene heterostructures can achieve on-off ratios up to 10^{12} while simultaneously enabling high current valley polarization, making them promising candidates for valleytronic current switches [58].

The combined effects of strain and magnetic fields on conductance in graphene superlattices offer promising pathways for device applications. Strain-induced pseudomagnetic fields can be tailored by pressure to achieve directionally selective electronic transmission and valley filtering, realizing basic elements for valleytronics [59]. The ability to suppress Klein tunnelling through strain engineering addresses one of the fundamental challenges in graphene-based transistors, where the absence of backscattering typically prevents effective current switching [58]. Conductance modulation through the interplay of electrostatic barriers, magnetic fields, and mechanical deformations thus provides a versatile framework for controlling electron transport in graphene, with implications for flexible electronics, strain sensors, and quantum computing platforms [23, 56, 57].

4 Results and discussion

In this section, we analyze the case of a single magnetic and electrostatic barrier that allows us to obtain exact expressions with the possibility of corroboration of numerical calculations using the matrix transfer method from more than one barrier. Later, we consider the case of multiple barriers where the transmission is numerically calculated by using the matrix transfer method and Landauer-Büttiker formalism.

4.1 Analytic case: a single magnetic and electrostatic barrier

To obtain an explicit equation for the transmission and reflection coefficients, we will consider the case of a single magnetic and electrostatic barrier ($N = 1$) at $x_0 = 0$ and width D . From the left-hand side of (32), it follows

$$\rho_x = (e^{i\theta(\vec{k}_1^r)} - e^{i\theta(\vec{k}_1^t)})^{-1} \left((e^{-i\xi_{10}^t} e^{i\theta(\vec{k}_1^r)} - e^{-i\xi_{10}^r} e^{i\theta(\vec{k}_1^t)}) + \lambda_0 \lambda_1 e^{i\theta(\vec{k}_0^t)} (e^{-i\xi_{10}^r} - e^{-i\xi_{10}^t}) \right), \quad (35)$$

$$\rho_y = (e^{i\theta(\vec{k}_1^r)} - e^{i\theta(\vec{k}_1^t)})^{-1} \left(\lambda_1 e^{i\theta(\vec{k}_1^t)} e^{i\theta(\vec{k}_1^r)} (e^{-i\xi_{10}^t} - e^{-i\xi_{10}^r}) + \lambda_0 e^{i\theta(\vec{k}_0^t)} (e^{i\theta(\vec{k}_1^r)} e^{i\xi_{10}^r} - e^{i\theta(\vec{k}_1^t)} e^{-i\xi_{10}^t}) \right), \quad (36)$$

where we have made the identification $\xi_{10}^{(r/t)} = k_{x,1}^{(r/t)} D$, $\vec{k}_2^t = \vec{k}_0^t$ and $\lambda_2 = \lambda_0$ for $x > x_1$.

Now, assuming the following approximation for the pseudo-spin angle of the transmitted and reflected waves:

$$\theta(\vec{k}_n^r) = \pi - \theta(\vec{k}_n^t), \quad n = 0, 1, \quad (37)$$

and taking into account the sign change between the x component of the wave vectors $\vec{k}_n^{(r/t)}$ in each region, we obtain:

$$T = \frac{(v_x^2 k_{x,0}^t k_{x,1}^t)^2}{(v_x^2 k_{x,0}^t k_{x,1}^t \cos(k_{x,1}^t D))^2 + \left(v_y^2 k_{y,0} \left(k_{y,0} + \frac{eA_y(x)}{\hbar}\right) - \lambda_0 \lambda_1 |g(\vec{k}_0^t)| |g(\vec{k}_1^t)|\right)^2 \sin^2(k_{x,1}^t D)}, \quad (38)$$

$$R = \frac{v_y^2 \left(|g(\vec{k}_1^t)| k_{y,0} - \lambda_0 \lambda_1 |g(\vec{k}_0^t)| \left(k_{y,0} + \frac{eA_y(x)}{\hbar}\right)\right)^2 \sin^2(k_{x,1}^t D)}{(v_x^2 k_{x,0}^t k_{x,1}^t \cos(k_{x,1}^t D))^2 + \left(v_y^2 k_{y,0} \left(k_{y,0} + \frac{eA_y(x)}{\hbar}\right) - \lambda_0 \lambda_1 |g(\vec{k}_0^t)| |g(\vec{k}_1^t)|\right)^2 \sin^2(k_{x,1}^t D)}, \quad (39)$$

where $g(\vec{k}_0^t) = v_x k_{x,0}^t + i v_y k_{y,0}$ and $g(\vec{k}_1^t) = v_x k_{x,1}^t + i v_y \left(k_{y,0} + \frac{eA_y(x)}{\hbar}\right)$. For pristine graphene, previous results coincide with those in [4, 30, 60] when $B = 0$ or in [61] for $V_0 = 0$, respectively. In Eq. (39), it is possible to establish the condition for the anomalous Klein tunnelling angle, which is different from the Fabry-Pérot resonances. When $R = 0$, we find that

$$\sin \phi_{\text{KT}} = -\frac{e v_y A_y(x)}{V_0}, \quad (40)$$

such an incidence angle $\phi_0 = \phi_{\text{KT}}$ indicates the direction of perfect transmission, which also matches the refraction angle $\phi_t = \phi_0 = \phi_{\text{KT}}$ within the barrier. Therefore, this anomalous Klein tunnelling occurs when a ballistic electron inside the electrostatic and magnetic barriers keeps the beam trajectory straight.

To contrast the effect in the coefficient transmission and conductance of uniaxial deformation applied along the \mathcal{ZZ} and \mathcal{AC} directions, let us consider a system with a single potential barrier of height $V_0 = 14$ meV and width $D = \ell_B \approx 81.1$ nm under the influence of a δ -function magnetic barrier of strength $B = 0.1$ T at the same region (see Fig. 4).

As is well known, Klein tunnelling is identified in the pristine case when perfect transmission ($T = 1$) occurs for all values of incident energy E at $\phi_0 = 0^\circ$ (normal incidence). However, if we introduce a mechanical deformation along the \mathcal{ZZ} or \mathcal{AC} direction, we observe a modification in such a tunnelling. This fact is particularly evident in panels (a) and (b) in Fig. 4, where $T = 1$ does not occur at zero angle. Furthermore, comparing with the pristine graphene case under the interaction of magnetic and electrostatic barriers [61], the deformation along the \mathcal{ZZ} direction is more susceptible to deviating from the pristine case than along the \mathcal{AC} direction (see again Fig. 4).

Now, let us compare the panels (a) and (b) in Fig. 4 that correspond to two different configurations of mechanical deformations: along the \mathcal{ZZ} and \mathcal{AC} directions, respectively. These transmissions reveal that for $E = 10, 20, 30$ meV, the incidence angle for which the perfect transmission occurs in Fig. 4b lies closer to $\phi_0 = 0^\circ$ than in Fig. 4a. Actually, according to Eq. (40), for Fig. 4a, $\phi_{\text{KT}} \approx -36.04^\circ$ while for Fig. 4b, $\phi_{\text{KT}} \approx -31.70^\circ$. Moreover, for the incident energy $E = 30$ meV, the first one displays a large interval of angles ϕ_0 for which the perfect transmission is possible, in clear contrast to Fig. 4b, whose transmission profile is almost similar to the graphs for $E = 10, 20$ meV.

On the other hand, by comparing panels (c) and (d) in Fig. 4 –also obtained for mechanical deformations applied to the \mathcal{ZZ} and \mathcal{AC} directions, respectively– we can see that for the incidence angle $\phi_0 = 0^\circ$, transmission coefficient reaches a local minimum value that lies between energies $E = 10$ and $E = 20$ meV in both panels (almost within the energy scale in the graph). However, the minimum transmission is about $T = 0.3$ in Fig. 4c and around $T = 0.5$ in Fig. 4d. For $\phi_0 = 30^\circ$, the transmission coefficient in both figures starts to decrease from an energy close to $E = -10$ meV and almost reaches zero transmission near $E = 20$ meV, but then in Fig. 4c it starts to increase more rapidly than in Fig. 4d. Finally, for $\phi_0 = 80^\circ$, panel (c) exhibits two resonances, while panel (d) shows only one; in both, the transmission coefficient vanishes for some $E > 0$ exhibiting minigaps in wider regions in this last panel, in contrast to the first one.

Overall, in Figs. 4c and 4d, we observe that $T = 1$ is reached at negative oblique angles as a consequence of resonances within the chosen energy range and the mechanical deformation applied. Moreover, for all three angles used, transmission coefficient in panel (c) decreases more sharply at positive Fermi energies than in panel (d). As we said before, the anomalous Klein tunnelling appears at the incidence angle $\phi_{\text{KT}} \approx -36.04^\circ$ and $\phi_{\text{KT}} \approx -31.70^\circ$ for the direction of \mathcal{ZZ} and \mathcal{AC} direction, respectively, which is unaffected by modulating the Fermi level. The occurrence of anomalous Klein tunnelling is due to the conservation of pseudo-spin for these incidence angles, and it is only changed through the modulation of the magnetic field B and the electrostatic potential V_0 , as (40) establishes. As shown in Fig. 4c and 4d, other values of $T = 1$ are obtained by constructive interference inside the barrier giving rise to Fabry-Pérot

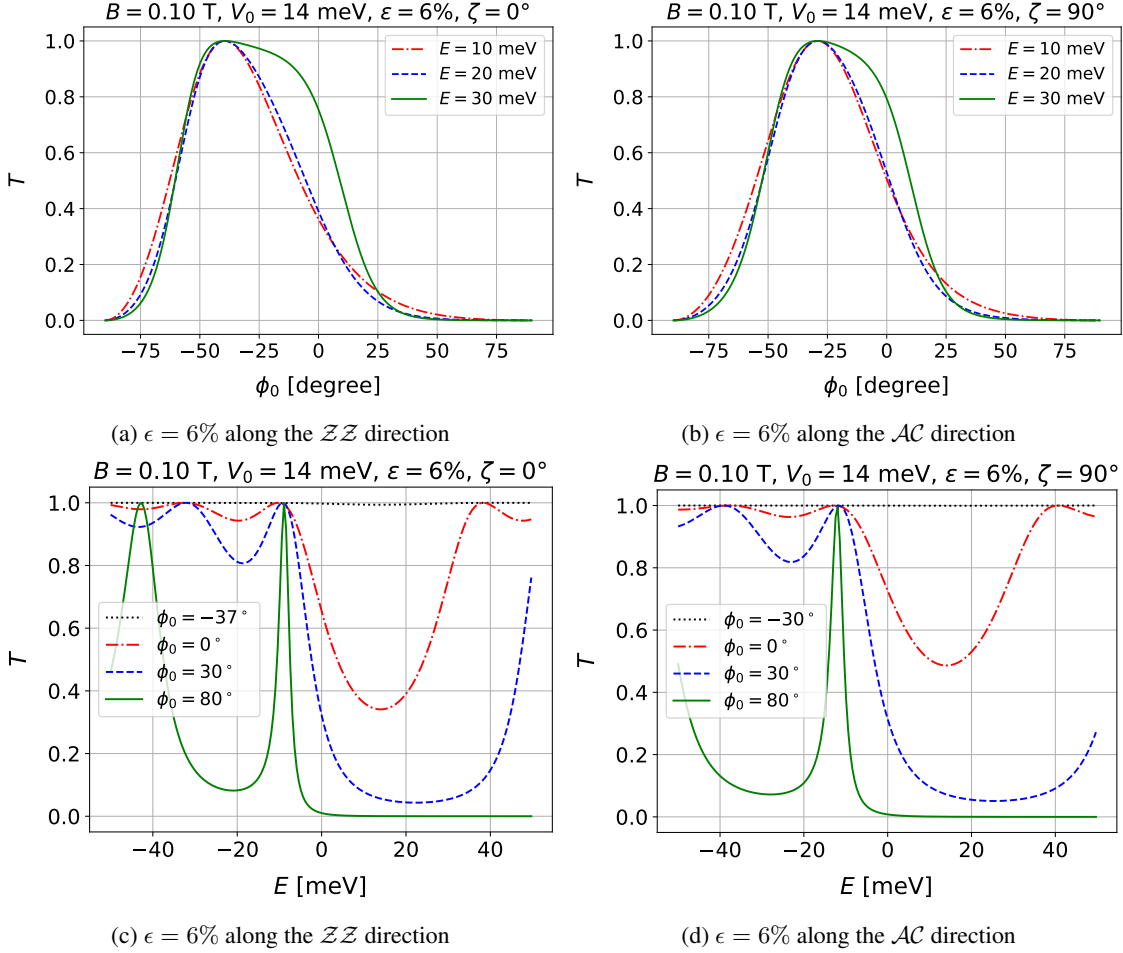


Figure 4: Electron transmission T in uniaxially strained graphene with a single electrostatic and magnetic barrier. Panels (a) and (b) show the dependence on the incidence angle ϕ_0 for different values of incident energy E . Panels (c) and (d) present the dependence on the Fermi energy E for different incidence angles ϕ_0 . The electrostatic barrier height is fixed at $V_0 = 14$ meV, while the magnetic field strength is set to $B = 0.1$ T, with a width $D \approx 81.1$ nm for both. The black-dotted line in the lower graphs corresponds to anomalous Klein tunnelling.

resonances. Such resonances are controlled by changing the width or height barrier as well as the tuning of the Fermi level.

Now, let us compare the behavior of the conductance of Eq. (33) in the pristine and strained graphene case. In Fig. 5a, strained graphene with $\epsilon = 6\%$ along the \mathcal{ZZ} direction exhibits the highest conductance, whereas strain along the \mathcal{AC} direction leads to the lowest values. The conductance of the pristine graphene lies between these two cases. In contrast, Fig. 5b shows the opposite behavior when a compress deformation is applied to the material: deformed graphene with $\epsilon = -6\%$ along the \mathcal{AC} direction exhibits the highest conductance, whereas with $\epsilon = -6\%$ along the \mathcal{ZZ} direction leads to the lowest values. This apparent interchange of the curves can be attributed to how the mechanical deformation modifies the crystalline structure, hopping parameters and, consequently, Fermi velocities in graphene. Then, when the magnetic field strength increases, the conductance is also modified as shown in Figs. 5c and 5d. More precisely, for a magnetic field strength $B = 0.1$ T and for a given Fermi energy value E , the conductance obtained depends on the mechanical deformation applied and is always different between the pristine and strained graphene cases. However, when $B = 0.2$ T, for instance, in the plots presented, resistance increases for $E > 0$, as shown in Fig. 5d. Furthermore, there are some values of incident energy E for which the conductance is the same in the pristine and strained graphene cases, as a consequence of the increase of B .

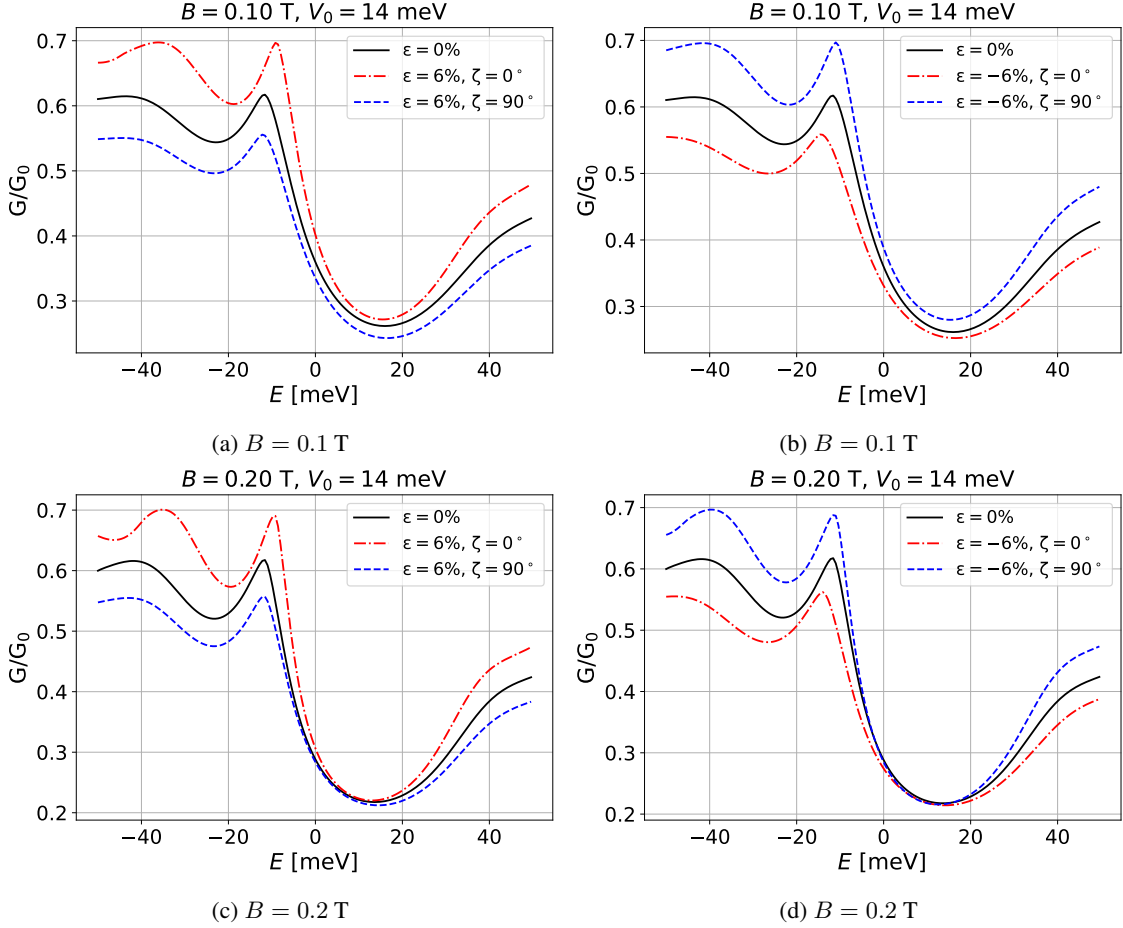


Figure 5: Conductance G/G_0 as a function of the Fermi level E for a single electrostatic and magnetic barrier. The solid black, dashed red, and dotted blue curves correspond to pristine graphene and to strained graphene along the ZZ and AC directions, respectively. The parameters are set as $V_0 = 14$ meV and $D \approx 81.1$ nm.

4.1.1 Fabry-Pérot resonances and critical angle

Delving deeper into the resonances that occur for oblique incidence ($\phi_0 \neq 0^\circ$), we recognize that a potential barrier can be analyzed as a double interface placed at $x = 0$ and $x_1 = D$, in analogy to a Fabry-Pérot interferometer [4]. Therefore, if the incoming wave interferes constructively with itself between the two interfaces, transmission resonances will occur since the barrier will be transparent for electrons with $k_{x,1}^t = n\pi/D$ (tunnelling resonance). More explicitly, the condition of such resonances is written as:

$$\left(\frac{n\pi}{D}\right)^2 = \left(\frac{E - V_0}{\hbar v_x}\right)^2 - \left(\frac{|E| \tan(\phi_0)}{\hbar v_y \sqrt{1 + \left(\frac{v_x \tan(\phi_0)}{v_y}\right)^2}} + \frac{e v_y A_y(x)}{\hbar v_x}\right)^2, \quad (41)$$

according to (20) and (21) (see Fig. 6).

Moreover, for certain incidence energies, there exists a critical incidence angle ϕ_c at which the x component of the transmitted wave vector \vec{k}_1^t becomes imaginary, causing the incident plane waves to become evanescent as they propagate inside the barrier. The condition that determines such a critical angle is:

$$\phi_c = \arcsin \left| \frac{v_y (E - V_0 - e v_y A_y(x))}{\sqrt{v_x^2 E^2 + (v_y^2 - v_x^2) (E - V_0 - e v_y A_y(x))^2}} \right|. \quad (42)$$

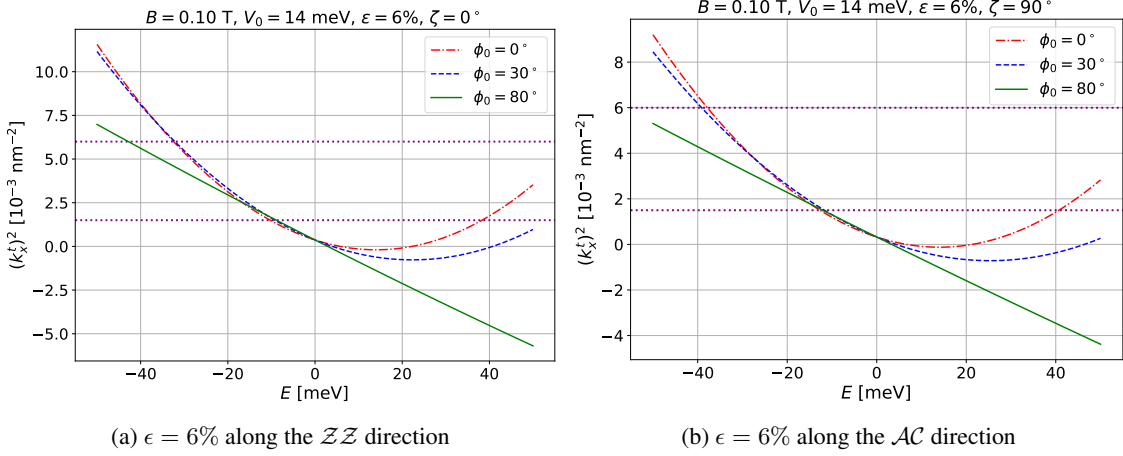


Figure 6: Behavior of the squared x -component of the transmitted wave number k_x^t in terms of the Fermi level E for some incidence angles ϕ_0 and different deformation configurations along the \mathcal{ZZ} and \mathcal{AC} directions. Horizontal purple dotted lines correspond to the values $n^2\pi^2/D^2$. tunnelling resonances are obtained when $k_{x,1}^t = n\pi/D$, as shown in Eq. (41).

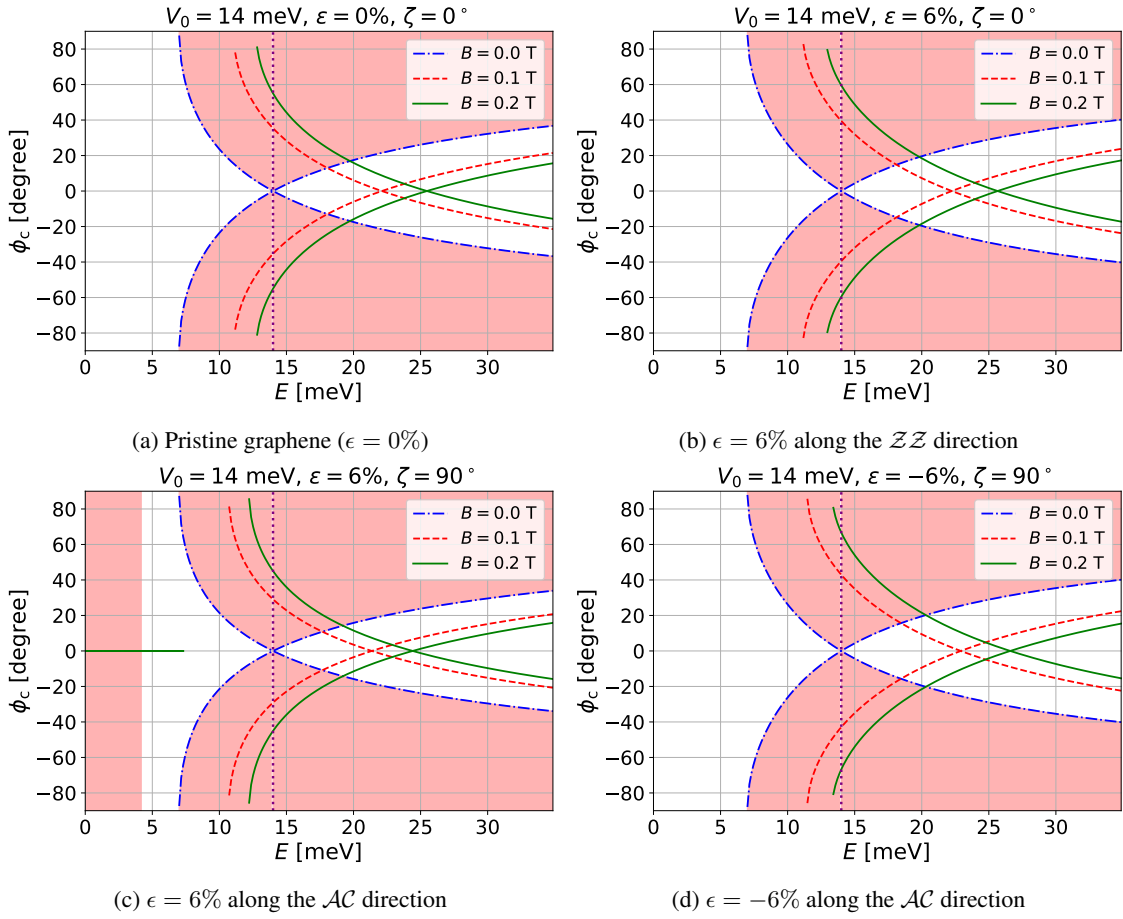


Figure 7: Phase diagram for the wave nature inside a magnetic and electrostatic barrier according to the incidence angle ϕ_c in (42) for different deformation configurations along the \mathcal{ZZ} or \mathcal{AC} direction and different magnetic field strengths B . In all cases, we set $V_0 = 14$ meV (vertical purple-dotted line). White regions identified the zone of oscillating waves, while red regions are the zone of evanescent waves.

Thus, electrons with an energy E for which there is no critical angle (i.e., the absolute value of the argument in (42) is greater than 1) cannot undergo total reflection at the barrier and are transmitted as plane waves. For an incident particle whose energy E guarantees that the absolute value of the argument in (42) is less than 1, it can only be transmitted as a plane wave if its incidence angle satisfies $|\phi_0| < \phi_c$, where the value of ϕ_c is determined by energy itself (see Fig. 7).

In other words, without a magnetic field, there is a zone of oscillating waves, or classically allowed region, for particles with incident energy $E < V_0/2$ that makes possible resonances and whose area reduces when $1/2 < E/V_0 < 1$. Additionally, there is a zone of evanescent waves, or classically forbidden, that provides the possibility of a tunnel effect via an evanescent wave. These regions are identified as white and red areas, respectively, in Fig. 7a, which correspond to the pristine case. The critical angle in Eq. (42) (blue curve in Fig. 7) delimits the areas of such regions, which can also be modified when a mechanical deformation is applied to the material (see Figs. 7b - 7d). When a magnetic field is applied (red and green curves in Fig. 7), the condition $E < V_0/2$ for oscillating waves is not fulfilled, and the regions described previously are displaced to the right, corresponding to larger energy values.

4.2 Numerical case: multi-barrier structure

Let us consider a uniform set of electrostatic potential barriers of height $V_0 = 14$ meV and δ -magnetic barriers of strength $B = 0.1$ T with width D and separation L equal to $\ell_B \approx 81.1$ nm, as illustrated in Fig. 3.

Here, Figs. 8 and 9 show the behavior of transmission coefficient as a function of the incidence angle ϕ_0 and Fermi energy E for different values of N , considering strained graphene at $\epsilon = 6\%$ (tensile deformation) and $\epsilon = -6\%$ (compress deformation), respectively, along the \mathcal{ZZ} ($\zeta = 0^\circ$) and \mathcal{AC} ($\zeta = 90^\circ$) direction. In general, for $N = 2$ to $N = 5$, it can be observed that the number of bands and minigaps increases with the number of barriers. In addition, in all cases studied in this section, it can be appreciated that the behavior described in the single-barrier section is preserved, namely, the absence of a Klein tunnelling at $\phi_0 = 0^\circ$ and the emergence of anomalous Klein tunnelling for different incidence angles.

On the other hand, when we compare the deformation along the \mathcal{ZZ} direction (first column) with that along the \mathcal{AC} direction (second column) in Fig. 8, we find notable differences between them. For instance, in the first case, anomalous Klein tunnelling appears in the interval $-40^\circ < \phi_{KT} < -35^\circ$, while in the second one, such an effect occurs in the range of $-32^\circ < \phi_{KT} < -27^\circ$, which is in agreement with the results shown in Figs. 4a and 4b for a single barrier. Moreover, such behavior persists as the number of barriers increases. In addition, it is clear at this point that, independent of the number of barriers, the incidence angle for which the anomalous Klein tunnelling appears closer to the normal incidence for tensile deformations along the \mathcal{AC} direction. In comparison with the pristine case [3, 4], the transmission coefficient suffers less modification when the tensile deformation is applied along \mathcal{AC} than when it occurs along the orthogonal direction, and the material is under the interaction of magnetic barriers. Then, when a compression is applied, as shown in Fig. 9, the above behaviors exchange with each other, resulting in a minor change in electron transmission T (compared to the pristine case) when such a mechanical deformation is applied along the \mathcal{ZZ} direction. Indeed, according to Eq. (40), for the values in Fig. 9, anomalous Klein tunnelling appears at $\phi_{KT} \approx -34.76^\circ$ for compression deformations along the \mathcal{ZZ} direction, while $\phi_{KT} \approx -39.50^\circ$ when the compression is applied along the \mathcal{AC} direction. Compared to a single-barrier case, this anomalous Klein tunnelling angle persists in the multiple-barrier structure because it is composed of a sequence of identical barriers, which are characterized by the same electrostatic potential height V_0 and the vector potential profile $\vec{A}(x)$. Consequently, Eq. (40) remains applicable to a system of multiple identical barriers. This robustness is due to the conservation of pseudospin, which holds equally in regions with and without external potentials. As a result, the electron beam maintains a straight line propagation across the entire multi-barrier structure.

Now, let us focus on the conductance behavior, which is shown in Fig. 10. For $N = 2$ to $N = 5$, the number of peaks in which the conductance reaches maximum values increases as the number of barriers N does. In all cases and in comparison to the pristine case, conductance tends to increase when a tensile deformation is applied along the \mathcal{ZZ} direction. In contrast, resistance tends to increase when such deformation acts on the orthogonal direction. Similar to the single-barrier case, the conductance exhibits a pronounced drop near $E = 0$ meV; however, it begins to increase again once $E > 20$ meV, approximately. On the other hand, although the conductance behavior observed in the single-barrier case is not as clear here, since the pristine conductance does not lie between the other two cases but intersects with the other conductance curves for given values of the Fermi energy, the general effect of a growing magnetic field strength is to increase resistance. This result can be understood considering that, though the configuration of the magnetic barriers does not allow Landau levels due to the abrupt change in the magnetic field profile, their action is sufficient to alter the dynamics of the charged particles, modifying the constructive interference in each region that the electron traverses.

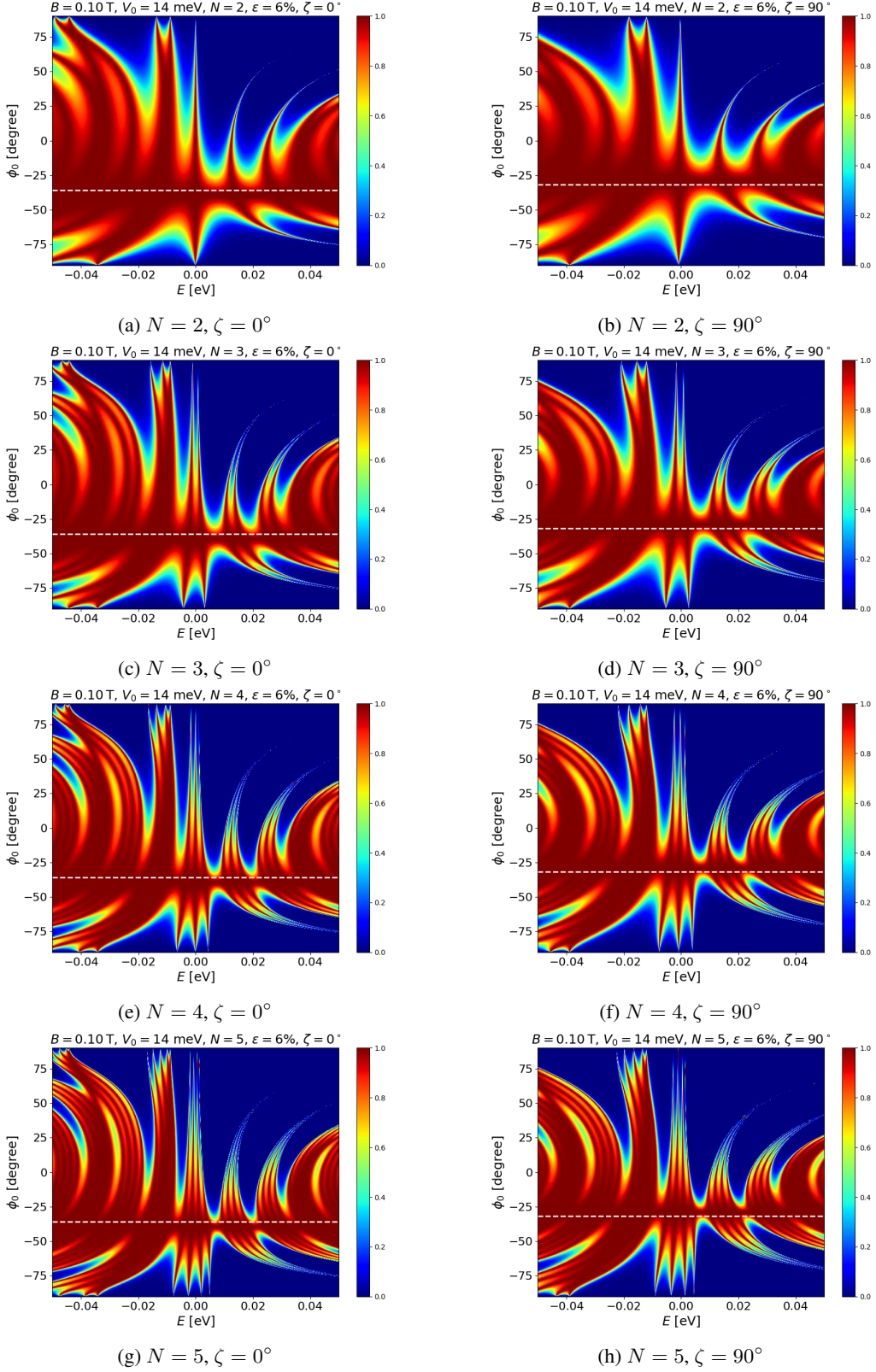


Figure 8: Electron transmission T in uniaxially strained graphene with $\epsilon = 6\%$, as a function of the Fermi energy E and the incidence angle ϕ_0 , for different numbers N of electrostatic and magnetic barriers. The LHS panels correspond to deformations along the \mathcal{ZZ} direction, while the RHS panels correspond to deformations along the \mathcal{AC} direction. In all cases, the parameters are set to $V_0 = 14$ meV, $B = 0.1$ T, and $L = D \approx 81.1$ nm. The dashed white line indicates the anomalous Klein tunnelling direction that occurs for the angle predicted in Eq. (40).

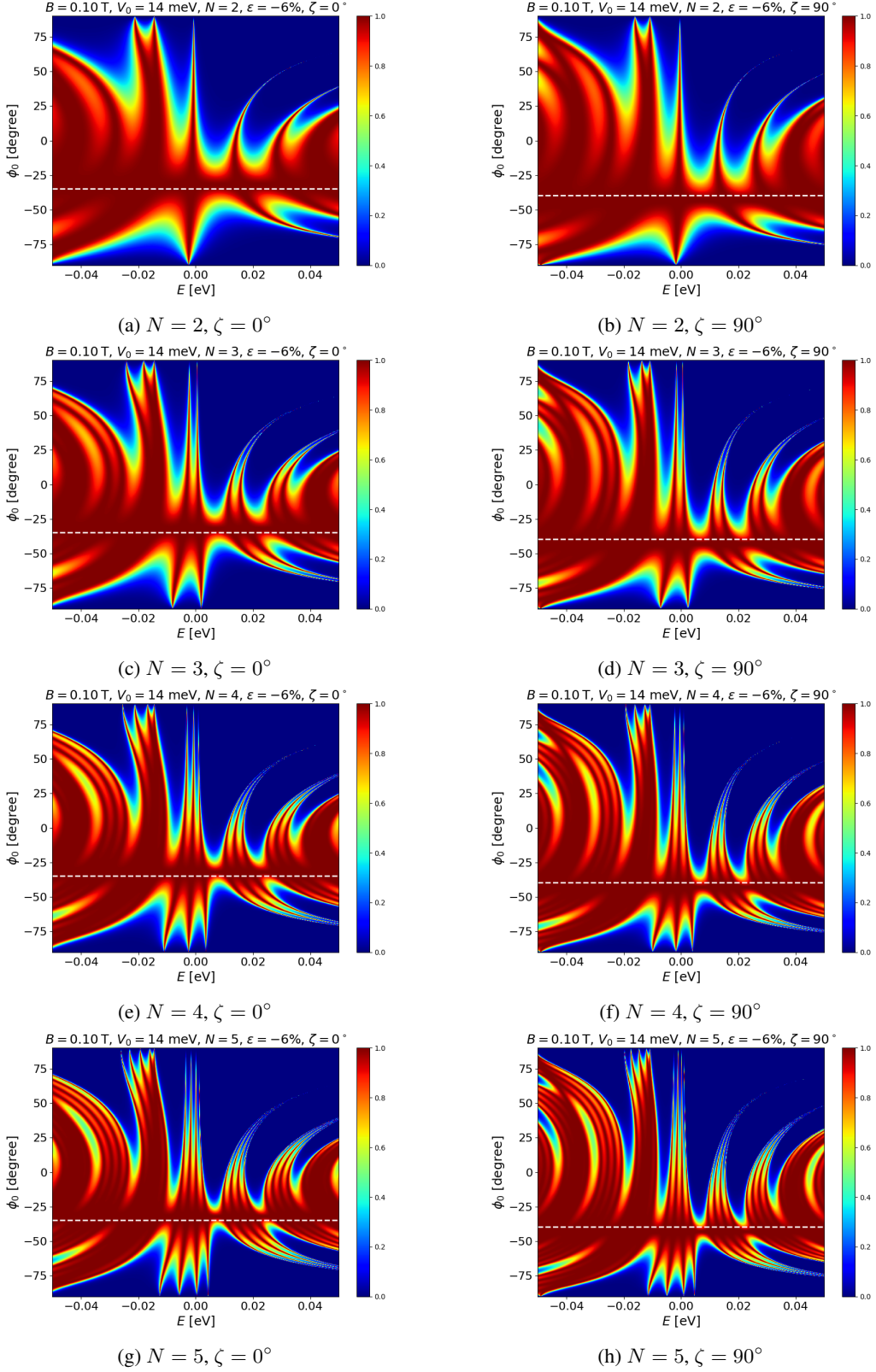


Figure 9: Electron transmission T in uniaxially strained graphene with $\epsilon = -6\%$, as a function of the Fermi energy E and the incidence angle ϕ_0 , for different numbers N of electrostatic and magnetic barriers. The LHS panels correspond to deformations along the \mathcal{ZZ} direction, while the RHS panels correspond to deformations along the \mathcal{AC} direction. In all cases, the parameters are set to $V_0 = 14$ meV, $B = 0.1$ T, and $L = D \approx 81.1$ nm. The dashed white line indicates the anomalous Klein tunnelling direction that occurs for the angle predicted in Eq. (40).

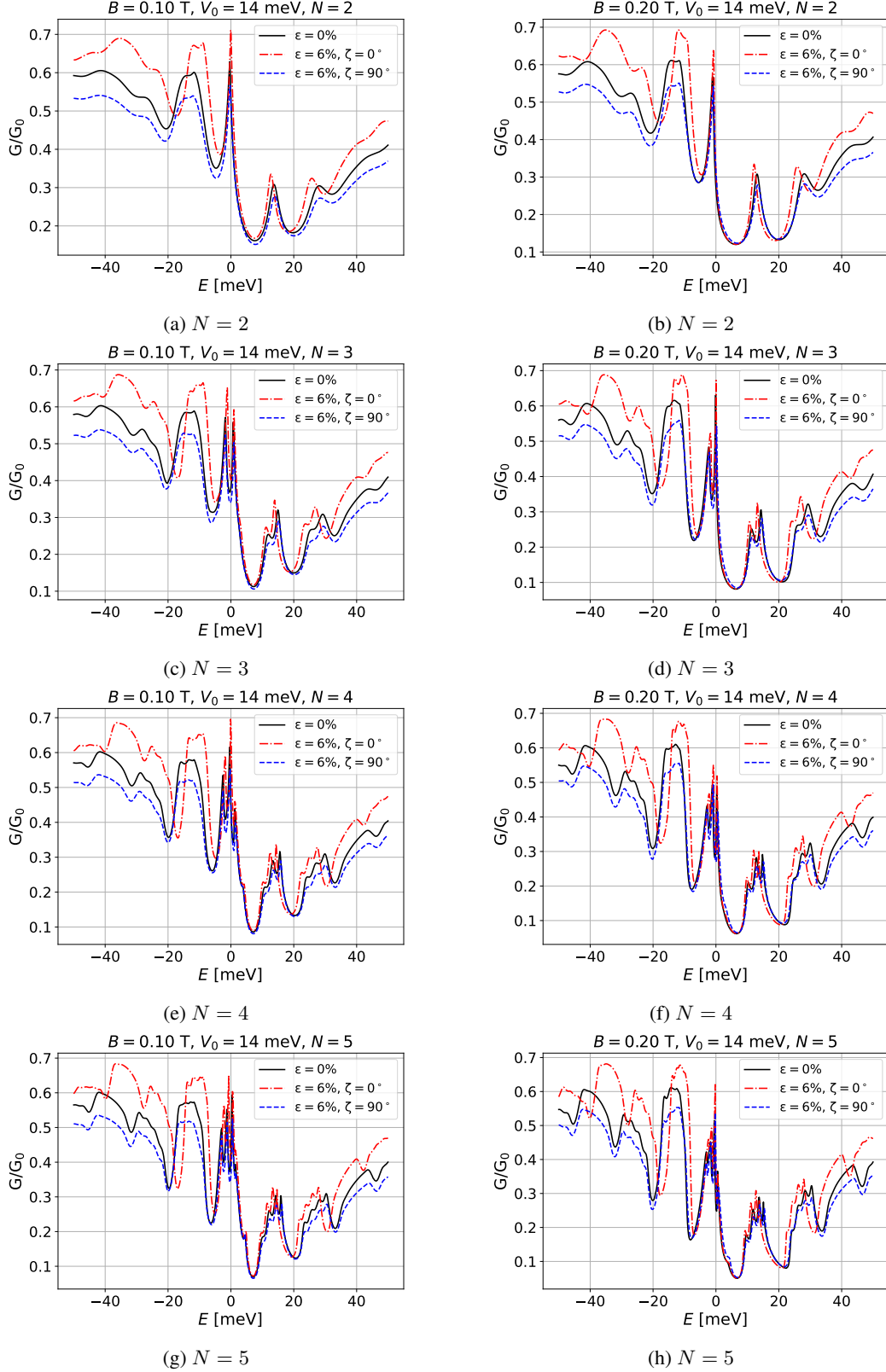


Figure 10: Conductance G/G_0 as a function of the Fermi level E for different numbers $N \geq 2$ of electrostatic and magnetic barriers with a fixed width $D \approx 81.1$ nm. The solid black, dashed red, and dotted blue curves correspond to pristine graphene and to strained graphene along the $\mathcal{Z}\mathcal{Z}$ and $\mathcal{A}\mathcal{C}$ directions, respectively. In all cases, the parameters are set to $V_0 = 14$ meV and $B = 0.1$ T ($B = 0.2$ T) for LHS (RHS) panels.

5 Conclusions

In this work, through the construction of a transfer matrix framework for a multi-barrier system composed of magnetic and electrostatic potentials, we describe the electron transmission of Dirac fermions in uniaxially strained graphene. This enables a major comprehension of how strain-engineering can be combined with magnetic interactions to modulate electron properties in graphene, for instance.

Our results show that, in general, an anomalous Klein tunnelling arises as a consequence of mechanical deformations applied to the material, as well as a set of δ -function magnetic barriers placed along a spatial direction on the material surface. In contrast to the usual anomalous Klein tunnelling [26, 35, 62], which occurs, for instance, when a mechanical deformation is applied in an oblique direction with respect to the \mathcal{ZZ} and \mathcal{AC} directions [35], here, such tunnelling can also be modulated via δ -function magnetic field barriers. Moreover, conductance is affected by the combined effect of strain and the magnetic field applied.

It is important to remark that although, as Fig. 2 suggests, tensile deformations along \mathcal{ZZ} direction can be considered as analogues to compress deformations along the \mathcal{AC} direction, and vice versa, as a result of the Poisson ratio of graphene, and this is observed in Figs. 5a and 5b for conductance, when the strength of magnetic barriers is modified, such equivalence is not fulfilled, as shown in Fig. 5d. This fact is also obtained when the RHS panels in Fig. 8 are compared with the LHS ones in Fig. 9, where the minibands and minigaps do not occur for the same Fermi energies, as well as the anomalous Klein tunnelling.

Now, while our model provides valuable insights into the combined effects of strain and magnetic barriers on Klein tunnelling, we acknowledge certain approximations that constrain its direct quantitative comparison with experiments. In particular, the continuum Dirac description assumes negligible valley mixing, which is valid for smooth potential variations but breaks down for atomic-scale disorder or sharp defects. Additionally, the δ -function magnetic barriers, while mathematically convenient, neglect Landau level formation and quantum confinement effects that would emerge in realistic finite-width barriers. Extensive theoretical work has investigated the trapping and confinement of Dirac-like electrons by inhomogeneous magnetic fields in graphene [47, 63–66]. These studies have shown that magnetic field inhomogeneities can create localized states and quantum dot behavior, effects that are not captured by the δ -function model. For a more quantitative description of realistic experimental setups where magnetic barriers have finite width, the model would need to be extended to include the spatial structure of the magnetic field and the resulting formation of edge states and quasi-bound states [67].

Despite its intrinsic limitations, the δ -function barrier model provides valuable physical insight into the interplay between magnetic confinement, strain-induced anisotropy, and Klein tunnelling. It serves as a useful pedagogical tool and offers qualitative guidance for understanding how magnetic field gradients can modulate electronic transport in strained graphene. In literature, it is reported that δ -function magnetic barriers could be achieved by applying ferromagnetic stripes following, for instance, a Kronig-Penney model [55, 68–70], and some results indicate that these types of structures enable modulation of electron valley polarization in graphene [71].

In summary, we consider that this study may help deepen understanding of how anisotropy and external magnetic fields together affect electron transmission and conductance in materials like graphene. Future theoretical work incorporating quantum confinement effects due to finite-width barriers, along with experimental studies on strain-engineered graphene devices with controlled magnetic field landscapes, would provide a more complete picture of anomalous Klein tunnelling in two-dimensional Dirac materials.

Acknowledgments

E.D.-B. and A.R. acknowledge financial support from CONAHCYT Project FORDECYT-PRONACES/61533/2020. They also acknowledge support from SIP-IPN under Grant No. 20254000 and CIC-UMSNH under Grant 18236, respectively. Y.B.-O. acknowledges financial support from UNAM-PAPIIT under the Project IA-102125.

References

- [1] O. Klein, “Die Reflexion von Elektronen an einem Potentialsprung nach der relativistischen Dynamik von Dirac,” *Zeitschrift für Physik*, vol. 53, pp. 157–165, 1929.
- [2] K. S. Novoselov, A. K. Geim, S. V. Morozov, D. Jiang, M. I. Katsnelson, I. V. Grigorieva, S. V. Dubonos, and A. A. Firsov, “Two-dimensional gas of massless Dirac fermions in graphene,” *Nature*, vol. 438, pp. 197–200, 2005.

- [3] M. I. Katsnelson, K. S. Novoselov, and A. K. Geim, “Chiral tunnelling and the Klein paradox in graphene,” *Nature Physics*, vol. 2, pp. 620–625, 2006.
- [4] P. E. Allain and J. N. Fuchs, “Klein tunneling in graphene: optics with massless electrons,” *The European Physical Journal B*, vol. 83, p. 301, 2011.
- [5] A. F. Young and P. Kim, “Quantum interference and Klein tunnelling in graphene heterojunctions,” *Nature Physics*, vol. 5, pp. 222–226, 2009.
- [6] N. Stander, B. Huard, and D. Goldhaber-Gordon, “Evidence for Klein tunneling in graphene p-n junctions,” *Physical Review Letters*, vol. 102, p. 026807, 2009.
- [7] T. R. Robinson, “On Klein tunneling in graphene,” *American Journal of Physics*, vol. 80, pp. 141–147, 2012.
- [8] T. Yokoyama, “Controllable valley and spin transport in ferromagnetic silicene junctions,” *Physical Review B*, vol. 87, p. 241409, 2013.
- [9] V. M. Pereira, A. H. Castro Neto, and N. M. R. Peres, “Tight-binding approach to uniaxial strain in graphene,” *Physical Review B*, vol. 80, p. 045401, 2009.
- [10] F. Guinea, M. I. Katsnelson, and A. K. Geim, “Energy gaps and a zero-field quantum Hall effect in graphene by strain engineering,” *Nature Physics*, vol. 6, pp. 30–33, 2010.
- [11] I. Y. Sahalianov, T. M. Radchenko, V. A. Tatarsenko, G. Cuniberti, and Y. I. Prylutsky, “Straintronics in graphene: Extra large electronic band gap induced by tensile and shear strains,” *Journal of Applied Physics*, vol. 126, p. 054302, 2019.
- [12] J.-D. Lu, P. Xu, and D. Wang, “Valley-dependent electronic transport in a graphene-based magnetic-strained superlattice,” *Journal of Superconductivity and Novel Magnetism*, vol. 35, pp. 1629–1634, 2022.
- [13] C.-H. Park, L. Yang, Y.-W. Son, M. L. Cohen, and S. G. Louie, “Anisotropic behaviours of massless Dirac fermions in graphene under periodic potentials,” *Nature Physics*, vol. 4, pp. 213–217, 2008.
- [14] M. Barbier, P. Vasilopoulos, and F. M. Peeters, “Extra Dirac points in the energy spectrum for superlattices on single-layer graphene,” *Physical Review B*, vol. 81, p. 075438, 2010.
- [15] A. Sánchez-Arellano, J. Madrigal-Melchor, and I. Rodríguez-Vargas, “Non-conventional graphene superlattices as electron band-pass filters,” *Scientific Reports*, vol. 9, p. 8759, 2019.
- [16] M. Barbier, P. Vasilopoulos, and F. M. Peeters, “Single-layer and bilayer graphene superlattices: collimation, additional Dirac points and Dirac lines,” *Philosophical Transactions of the Royal Society A*, vol. 368, pp. 5499–5524, 2010.
- [17] M. Sharma and S. Ghosh, “Electron transport and Goos–Hänchen shift in graphene with electric and magnetic barriers: optical analogy and band structure,” *Journal of Physics: Condensed Matter*, vol. 23, no. 5, p. 055501, 2011.
- [18] M. Yankowitz, J. Xue, D. Cormode, J. D. Sanchez-Yamagishi, K. Watanabe, T. Taniguchi, P. Jarillo-Herrero, P. Jacquod, and B. J. LeRoy, “Emergence of superlattice Dirac points in graphene on hexagonal boron nitride,” *Nature Physics*, vol. 8, pp. 382–386, 2012.
- [19] L. A. Ponomarenko, R. V. Gorbachev, G. L. Yu, D. C. Elias, R. Jalil, A. A. Patel, A. Mishchenko, A. S. Mayorov, C. R. Woods, J. R. Wallbank, M. Mucha-Kruczynski, B. A. Piot, M. Potemski, I. V. Grigorieva, K. S. Novoselov, F. Guinea, V. I. Fal’ko, and A. K. Geim, “Cloning of Dirac fermions in graphene superlattices,” *Nature*, vol. 497, pp. 594–597, 2013.
- [20] C. R. Dean, L. Wang, P. Maher, C. Forsythe, F. Ghahari, Y. Gao, J. Katoch, M. Ishigami, P. Moon, M. Koshino, T. Taniguchi, K. Watanabe, K. L. Shepard, J. Hone, and P. Kim, “Hofstadter’s butterfly and the fractal quantum Hall effect in moiré superlattices,” *Nature*, vol. 497, pp. 598–602, 2013.
- [21] W. A. de Heer, C. Berger, X. Wu, P. N. First, E. H. Conrad, X. Li, T. Li, M. Sprinkle, J. Hass, M. L. Sadowski, M. Potemski, and G. Martinez, “Epitaxial graphene,” *Solid State Communications*, vol. 143, no. 1, pp. 92–100, 2007.
- [22] Y.-M. Lin, C. Dimitrakopoulos, K. A. Jenkins, D. B. Farmer, H.-Y. Chiu, A. Grill, and P. Avouris, “100-GHz Transistors from Wafer-Scale Epitaxial Graphene,” *Science*, vol. 327, p. 662, 2010.
- [23] F. Schwierz, “Graphene transistors,” *Nature Nanotechnology*, vol. 5, pp. 487–496, 2010.
- [24] M. Oliva-Leyva and G. G. Naumis, “Understanding electron behavior in strained graphene as a reciprocal space distortion,” *Physical Review B*, vol. 88, p. 085430, 2013.
- [25] D. Midtvedt, C. H. Lewenkopf, and A. Croy, “Strain–displacement relations for strain engineering in single-layer 2D materials,” *2D Mater.*, vol. 3, no. 1, p. 011005, 2016.

- [26] Y. Betancur-Ocampo, “Partial positive refraction in asymmetric Veselago lenses of uniaxially strained graphene,” *Physical Review B*, vol. 98, p. 205421, 2018.
- [27] M. O. Goerbig, “Electronic properties of graphene in a strong magnetic field,” *Rev. Mod. Phys.*, vol. 83, p. 1193, 2011.
- [28] M. O. Goerbig, J.-N. Fuchs, G. Montambaux, and F. Piéchon, “Tilted anisotropic Dirac cones in quinoid-type graphene and α -(BEDT-TTF)₂I₃,” *Physical Review B*, vol. 78, p. 045415, 2008.
- [29] P. R. Wallace, “The band theory of graphite,” *Phys. Rev.*, vol. 71, p. 622, 1947.
- [30] A. H. Castro Neto, F. Guinea, N. M. R. Peres, K. S. Novoselov, and A. K. Geim, “The electronic properties of graphene,” *Rev. Mod. Phys.*, vol. 81, p. 109, 2009.
- [31] D. A. Papaconstantopoulos, M. J. Mehl, S. C. Erwin, and M. R. Pederson, “Tight-Binding Hamiltonians for Carbon and Silicon,” *MRS Proceedings*, vol. 491, p. 221, 1997.
- [32] E. Díaz-Bautista and Y. Betancur-Ocampo, “Phase-space representation of Landau and electron coherent states for uniaxially strained graphene,” *Physical Review B*, vol. 101, p. 125402, Mar 2020.
- [33] V. M. Pereira and A. H. Castro Neto, “Strain Engineering of Graphene’s Electronic Structure,” *Phys. Rev. Lett.*, vol. 103, p. 046801, 2009.
- [34] E. Cadelano, P. L. Palla, S. Giordano, and L. Colombo, “Nonlinear Elasticity of Monolayer Graphene,” *Phys. Rev. Lett.*, vol. 102, p. 235502, 2009.
- [35] E. Díaz-Bautista, Y. Betancur-Ocampo, and A. Raya, “Extended transfer matrix method for electron transmission in anisotropic 2D materials: Interplay of strain and (a)periodicity of potentials,” *Journal of Applied Physics*, vol. 136, p. 124302, 09 2024.
- [36] T. Ando, “Theory of electronic states and transport in carbon nanotubes,” *Journal of the Physical Society of Japan*, vol. 74, pp. 777–817, 2005.
- [37] N. M. R. Peres, F. Guinea, and A. H. Castro Neto, “Electronic properties of disordered two-dimensional carbon,” *Physical Review B*, vol. 73, p. 125411, 2006.
- [38] K. Cao, S. Feng, Y. Han, L. Gao, T. H. Ly, Z. Xu, and Y. Lu, “Elastic straining of free-standing monolayer graphenes,” *Nature Communications*, vol. 11, p. 284, 2020.
- [39] C. R. Dean, A. F. Young, I. Meric, C. Lee, L. Wang, S. Sorgenfrei, K. Watanabe, T. Taniguchi, P. Kim, K. L. Shepard, and J. Hone, “Boron nitride substrates for high-quality graphene electronics,” *Nature Nanotechnology*, vol. 5, pp. 722–726, 2010.
- [40] L. Wang, I. Meric, P. Y. Huang, Q. Gao, Y. Gao, H. Tran, T. Taniguchi, K. Watanabe, L. M. Campos, D. A. Muller, J. Guo, P. Kim, J. Hone, K. L. Shepard, and C. R. Dean, “One-dimensional electrical contact to a two-dimensional material,” *Science*, vol. 342, pp. 614–617, 2013.
- [41] N. Leconte, A. Lherbier, F. Varchon, P. Ordejon, S. Roche, and J.-C. Charlier, “Quantum transport in chemically modified two-dimensional graphene: From minimal conductivity to Anderson localization,” *Phys. Rev. B*, vol. 84, p. 235420, Dec 2011.
- [42] M. Settnes, S. R. Power, and A.-P. Jauho, “Pseudomagnetic fields and triaxial strain in graphene,” *Physical Review B*, vol. 93, p. 035456, 2016.
- [43] Ícaro S.F. Bezerra and J. R. Lima, “Transport properties of magnetic graphene superlattices with modulated Fermi velocity,” *Solid State Communications*, vol. 340, p. 114511, 2021.
- [44] D. E. Fernandes, “Effective medium model for graphene superlattices with electrostatic and magnetic vector potentials,” *Physical Review B*, vol. 107, p. 085119, Feb 2023.
- [45] Y. Fattasse, M. Mekkaoui, A. Jellal, and A. Bahaoui, “Effect of strain on tunneling time in graphene magnetic barrier,” *Physica E: Low-dimensional Systems and Nanostructures*, vol. 148, p. 115634, 2023.
- [46] W. Belhadj, H. Dakhlaoui, O. H. Alsalami, and F. Urgan, “Impacts of electric and magnetic fields on the optical and electronic characteristics of graphene-based multibarrier structure,” *Optical and Quantum Electronics*, vol. 55, p. 1171, 2023.
- [47] A. De Martino, L. Dell’Anna, and R. Egger, “Magnetic barriers and confinement of Dirac–Weyl quasiparticles in graphene,” *Solid State Communications*, vol. 144, no. 12, pp. 547–550, 2007.
- [48] R. Landauer, “Spatial variation of currents and fields due to localized scatterers in metallic conduction,” *IBM Journal of Research and Development*, vol. 1, pp. 223–231, 1957.
- [49] M. Büttiker, “Four-terminal phase-coherent conductance,” *Physical Review Letters*, vol. 57, pp. 1761–1764, 1986.

- [50] S. Datta, *Electronic Transport in Mesoscopic Systems*. Cambridge University Press, 1995.
- [51] L. E. F. Foa Torres, S. Roche, and J.-C. Charlier, *Introduction to Graphene-Based Nanomaterials: From Electronic Structure to Quantum Transport*. Cambridge University Press, 2014.
- [52] J. Tworzydło, B. Trauzettel, M. Titov, A. Rycerz, and C. W. J. Beenakker, “Sub-Poissonian Shot Noise in Graphene,” *Physical Review Letters*, vol. 96, p. 246802, 2006.
- [53] B. Huard, J. A. Sulpizio, N. Stander, K. Todd, B. Yang, and D. Goldhaber-Gordon, “Transport measurements across a tunable potential barrier in graphene,” *Physical Review Letters*, vol. 98, p. 236803, 2007.
- [54] Y. Li, Q. Wan, Y. Peng, G. Wang, Z. Qian, G. Zhou, and M. B. A. Jalil, “The effect of magnetic field on chiral transmission in p-n-p graphene junctions,” *Scientific Reports*, vol. 5, p. 18458, 2016.
- [55] C. Yesilyurt, S. G. Tan, G. Liang, and M. B. A. Jalil, “Klein tunneling in Weyl semimetals under the influence of magnetic field,” *Scientific Reports*, vol. 6, p. 38862, 2016.
- [56] S. B. Kumar and J. Guo, “Strain-induced conductance modulation in graphene grain boundary,” *Nano Letters*, vol. 12, pp. 1362–1366, 3 2012.
- [57] V. H. Nguyen, H.-V. Nguyen, J. Saint-Martin, and P. Dollfus, “Strain-induced conduction gap in vertical devices made of misoriented graphene layers,” *Nanotechnology*, vol. 26, p. 115201, feb 2015.
- [58] M. Chauwin, Z. B. Siu, and M. B. A. Jalil, “Strain-modulated graphene heterostructure as a valleytronic current switch,” *Physical Review Applied*, vol. 17, p. 024035, 2022.
- [59] G. W. Jones, D. A. Bahamon, A. H. C. Neto, and V. M. Pereira, “Quantized transport, strain-induced perfectly conducting modes, and valley filtering on shape-optimized graphene corbino devices,” *Nano Letters*, vol. 17, pp. 5304–5313, 9 2017.
- [60] J. D. Lejarreta, C. H. Fuentevilla, E. Diez, and J. M. Cerveró, “An exact transmission coefficient with one and two barriers in graphene,” *Journal of Physics A: Mathematical and Theoretical*, vol. 46, p. 155304, apr 2013.
- [61] N. Myoung and G. Ihm, “Tunneling of Dirac fermions through magnetic barriers in graphene,” *Physica E: Low-dimensional Systems and Nanostructures*, vol. 42, no. 1, pp. 70–72, 2009.
- [62] X. Zhou, “Valley-dependent electron retroreflection and anomalous Klein tunneling in an 8- $Pmmn$ borophene-based $n-p-n$ junction,” *Physical Review B*, vol. 100, p. 195139, Nov 2019.
- [63] A. De Martino, L. Dell’Anna, and R. Egger, “Magnetic Confinement of Massless Dirac Fermions in Graphene,” *Phys. Rev. Lett.*, vol. 98, p. 066802, Feb 2007.
- [64] F. Libisch, S. Rotter, J. Güttinger, C. Stampfer, and J. Burgdörfer, “Transition to Landau levels in graphene quantum dots,” *Physical Review B*, vol. 81, no. 24, p. 245411, 2010.
- [65] L. Cohnitz, W. Häusler, A. Zazunov, and R. Egger, “Interaction-induced conductance from zero modes in a clean magnetic graphene waveguide,” *Phys. Rev. B*, vol. 92, p. 085422, Aug 2015.
- [66] M. Slota, A. Keerthi, W. K. Myers, E. Tretyakov, M. Baumgarten, A. Ardavan, H. Sadeghi, C. J. Lambert, A. Narita, K. Müllen, and L. Bogani, “Magnetic edge states and coherent manipulation of graphene nanoribbons,” *Nature*, vol. 557, pp. 691–695, 2018.
- [67] P. G. Silvestrov and K. B. Efetov, “Quantum dots in graphene,” *Physical Review Letters*, vol. 98, no. 1, p. 016802, 2007.
- [68] A. Matulis, F. M. Peeters, and P. Vasilopoulos, “Wave-vector-dependent tunneling through magnetic barriers,” *Phys. Rev. Lett.*, vol. 72, pp. 1518–1521, Mar 1994.
- [69] M. Ramezani Masir, P. Vasilopoulos, and F. M. Peeters, “Magnetic Kronig–Penney model for Dirac electrons in single-layer graphene,” *New Journal of Physics*, vol. 11, p. 095009, sep 2009.
- [70] C. Yesilyurt, S. Ghee Tan, G. Liang, and M. B. A. Jalil, “Perfect valley filter in strained graphene with single barrier region,” *AIP Advances*, vol. 6, p. 056303, 03 2016.
- [71] X.-S. Chen, D. Wang, P. Xu, and J.-D. Lu, “Effect of ferromagnetic metal stripe and strained barrier on electron transport characteristics in a graphene,” *Journal of Superconductivity and Novel Magnetism*, vol. 35, pp. 3363–3369, 2022.